

Active RIS-Assisted MIMO-OFDM System: Analyses and Prototype Measurements

De-Ming Chian, *Graduate Student Member, IEEE*, Feng-Ji Chen, Yu-Chen Chang, Chao-Kai Wen, *Senior Member, IEEE*, Chi-Hung Wu, Fu-Kang Wang, *Member, IEEE*, Kai-Kit Wong, *Fellow, IEEE*, and Chan-Byoung Chae, *Fellow, IEEE*

Abstract—In this study, we develop an active reconfigurable intelligent surface (RIS)-assisted multiple-input multiple-output orthogonal frequency division multiplexing (MIMO-OFDM) prototype compliant with the 5G New Radio standard at 3.5 GHz. The experimental results clearly indicate that active RIS plays a vital role in enhancing MIMO performance, surpassing passive RIS. Furthermore, when considering factors such as complexity, energy consumption, and performance, the comparative evaluation between passive RIS and active RIS reinforces the critical role of active RIS in MIMO systems. These findings underscore the practical significance of active RIS in improving MIMO gain in 5G scenarios.

Index Terms—Reconfigurable intelligent surface (RIS), active RIS, prototype, beamforming optimization.

I. INTRODUCTION

FUTURE wireless communication systems require advanced transceiver designs and support for dynamic wireless channel transformations. Reconfigurable Intelligent Surfaces (RIS) have emerged as a promising solution in achieving this goal. Extensive prototypes and experiments have been conducted in academia and industry, as evidenced by the works [1–8].

The current understanding of RIS channel characteristics suggests that the equivalent path loss of the RIS link can be approximated as the product of the path losses of the transmitter-RIS link and the RIS-receiver link, resulting in weaker multipath characteristics compared to the direct link. Traditional approaches involve equipping RIS with large reflecting elements, which introduce challenges in terms of channel estimation and real-time optimization of reflection coefficients [9].

To address these challenges, the concept of active RIS has been proposed, enabling simultaneous signal reflection and amplification. Active RIS systems, unlike passive RIS systems without signal amplification, provide more effective compensation for severe cascaded path loss [9–11]. An example of

D.-M. Chian, F.-J. Chen, Y.-C. Chang, and C.-K. Wen are with the Institute of Communications Engineering, National Sun Yat-sen University, Kaohsiung 804, Taiwan (e-mail: icefreeman123@gmail.com, king19635@gmail.com, william881106@gmail.com, chaokai.wen@mail.nsysu.edu.tw).

C.-H. Wu and F.-K. Wang are with the Department of Electrical Engineering, National Sun Yat-sen University, Kaohsiung 804, Taiwan (e-mail: yes121335@gmail.com, fkw@mail.ee.nsysu.edu.tw).

K.-K. Wong is with Department of Electronic and Electrical Engineering, University College London, UK, Email: kai-kit.wong@ucl.ac.uk. He is also affiliated with Yonsei Frontier Lab, Yonsei University, Korea.

C.-B. Chae is with the School of Integrated Technology, Yonsei University, Seoul 03722, Korea, Email: cbchae@yonsei.ac.kr.

an active RIS system can be seen in the photograph of a 64-element active RIS-aided wireless communication system developed in [12].

However, most RIS-assisted wireless communication prototypes and measurements have focused on single-input single-output (SISO) scenarios using horn antennas. This approach does not align with practical base station and smartphone form factors, particularly for Sub-6 GHz communications. There is a scarcity of information available regarding RIS-aided multiple-input multiple-output (MIMO) systems. This study aims to address this gap by presenting the results of an experimental demonstration of an active RIS-assisted MIMO-OFDM prototype operating at 3.5 GHz under the 5G New Radio (NR) standard. The key contributions of this study are as follows:

- It represents a significant milestone as the first experimental development of active RIS-assisted MIMO-OFDM within the context of 5G NR. It offers valuable insights into the practical implementation of RIS technology in MIMO systems.
- It implements practical RIS-assisted MIMO control algorithms, including codebook-based algorithms, conditional sample mean (CSM) [7], and blind greedy (BG) algorithms [8], within a unified platform. This implementation enables a direct comparison of various RIS-assisted MIMO methodologies through real-world tests.
- It provides a comprehensive comparative evaluation of passive RIS and active RIS with different RIS elements using various algorithms. By examining the trade-off between complexity, energy consumption, and performance, it sheds light on the differences and considerations associated with these RIS technologies.

The experimental results highlight the greater potential of active RIS over passive RIS, particularly in the context of MIMO systems.

II. DESIGN OF ACTIVE RIS

A. Active RIS Element

The structure of our “active RIS element”, as depicted in Fig. 1(a), consists of a receive antenna (rRIS) and N_d transmit antennas (tRIS). When an electromagnetic wave is incident on the rRIS, it passes through two low-noise amplifiers (LNAs) and an N_d -way power splitter (PS). Each of the N_d separated paths is then individually adjusted by a digital phase shifter (DPS) and subsequently radiated back into the air through

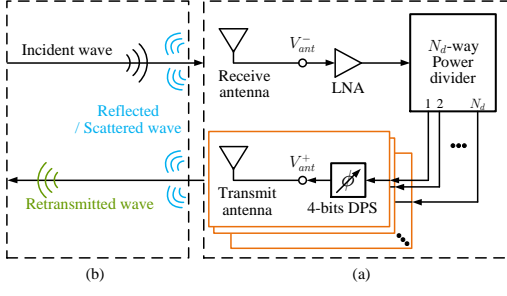


Fig. 1. (a) Active RIS element and (b) its channel model.

the N_d tRIS antennas. The rRIS and tRIS antennas are based on patch antenna technology, similar to the approach described in [8]. The operating center frequency of our system is 3.5 GHz. The DPS, MAPS-010144, is a 4-bit phase shifter manufactured by M/A-COM Technology Solutions Inc., capable of providing phase shifts ranging from 0° to 360° in steps of 22.5° . The LNA, ZX60-83LN-S+, with a gain of approximately 20 dB, and the PS, ZB8PD-622-S+, with 8 output ports, are sourced from Mini-Circuits International Inc.

By excluding the rRIS and tRIS elements in Fig. 1(a), the total transmission coefficient from the LNAs to the DPS can be expressed as

$$\Phi = \frac{V_{\text{ant}}^+}{V_{\text{ant}}^-} = \Phi_{\text{lna}} \cdot \Phi_{\text{ps}} \cdot \Phi_{\text{dps}}, \quad (1)$$

where V_{ant}^+ and $V_{\text{ant}}^- \in \mathbb{C}$ denote the signal traveling towards and away from the antenna port, respectively, and $\Phi_{\text{lna}}, \Phi_{\text{ps}}, \Phi_{\text{dps}} \in \mathbb{C}$ are the transmission coefficients of the LNA, PS, and DPS, respectively. For our hardware components, the magnitude of Φ , without considering the loss of the connection line, provides approximately an 8 dB gain due to a 9 dB loss from the PS and a 3 dB loss from the DPS, and the phase of Φ can be controlled by the DPS.

B. System Model

Next, we present the system model with the active RIS, aiming to introduce the corresponding performance metric of interest. We consider a 5G NR-compatible OFDM system. The transmission band consists of multiple subcarriers. Our channel modeling specifically targets each individual subcarrier, taking into account the number of antennas at the transmitter, denoted as N_t , and the number of antennas at the receiver, denoted as N_r . In our designed active RIS, we use K_{ris} active RIS elements, resulting in $K = K_{\text{ris}} \times N_d$ antennas for the RIS, as discussed in the previous subsection.

The transmit signal from the n_t -th Tx antenna at one of the subcarriers is represented as s^{n_t} . The transmitted signal vector from all Tx antennas can be denoted as $\mathbf{s} = [s^1, \dots, s^{N_t}]^T$. Following the approach in [8], the channel frequency response (CFR) is modeled by considering three types of paths in the RIS scenario:

- First, s^{n_t} propagates through the line-of-sight (LoS) path or paths that do not interact with the RIS.
- Second, when s^{n_t} is received by the k_r -th rRIS and retransmitted by the k_t -th tRIS, it undergoes propagation via the antenna mode (AM) of the RIS path.

- Third, when s^{n_t} impinges on the metal plate of the k_r -th rRIS or k_t -th tRIS and generates reflected and scattered signals towards the receiver, it experiences propagation via the structural mode (SM) of the RIS path.

The channel model for the second and third types of paths is illustrated in Fig. 1(b).

Consequently, the CFR of all paths at one of the subcarriers for the MIMO system is formulated as:

$$\mathbf{H} = \mathbf{H}_{\text{los}} + \mathbf{H}_{\text{am}} + \mathbf{H}_{\text{sm}}, \quad (2)$$

where \mathbf{H}_{los} , \mathbf{H}_{am} , and \mathbf{H}_{sm} correspond to the three types of paths, respectively. The AM of the RIS path can be expressed as:

$$\mathbf{H}_{\text{am}} = \mathbf{H}_{\text{am}}^{\text{r}} \cdot \Phi \cdot \mathbf{H}_{\text{am}}^{\text{t}}, \quad (3)$$

where $\Phi = \text{diag}(\Phi^1, \dots, \Phi^K)$, Φ^k represents the total transmission coefficient of the k -th tRIS element as described in (1), and $\mathbf{H}_{\text{am}}^{\text{r}}$ and $\mathbf{H}_{\text{am}}^{\text{t}}$ are the AM of the RIS paths corresponding to the receiver and transmitter, respectively. Then, the frequency domain representation of the received signal can be written as [11]:

$$\mathbf{y} = \mathbf{H}\mathbf{s} + \mathbf{H}_{\text{am}}^{\text{r}} \cdot \Phi \cdot \mathbf{H}_{\text{am}}^{\text{t}} \mathbf{v} + \mathbf{z}, \quad (4)$$

where $\mathbf{v} \sim \mathcal{CN}(\mathbf{0}_K, \sigma_v^2 \mathbf{I}_K)$ and $\mathbf{z} \sim \mathcal{CN}(\mathbf{0}_{N_r}, \sigma_z^2 \mathbf{I}_{N_r})$ represent the noise introduced by the active RIS and the receiver, respectively.

Since \mathbf{v} undergoes transmission through the MIMO channel, $\mathbf{n}_d \triangleq \mathbf{H}_{\text{am}}^{\text{r}} \cdot \Phi \mathbf{v}$ represents the colored noise. The total noise covariance matrix, denoted as $\mathbf{n} \triangleq \mathbf{n}_d + \mathbf{z}$, can be written as $\mathbf{R}_n = \mathbb{E}\{\mathbf{n}\mathbf{n}^H\} = \mathbf{R}_v + \sigma_z^2 \mathbf{I}_{N_r}$, where \mathbf{R}_v represents the covariance matrix of \mathbf{n}_d . Consequently, we can multiply \mathbf{y} by $\mathbf{R}_n^{-1/2}$ to whiten \mathbf{n} , resulting in

$$\tilde{\mathbf{y}} = \mathbf{R}_n^{-1/2} \mathbf{H}\mathbf{s} + \mathbf{R}_n^{-1/2} \mathbf{n} = \tilde{\mathbf{H}}\mathbf{s} + \tilde{\mathbf{n}}, \quad (5)$$

with $\tilde{\mathbf{H}} \triangleq \mathbf{R}_n^{-1/2} \mathbf{H}$, $\tilde{\mathbf{n}} \triangleq \mathbf{R}_n^{-1/2} \mathbf{n}$, and $\tilde{\mathbf{n}} \sim \mathcal{CN}(\mathbf{0}_{N_r}, \mathbf{I}_{N_r})$.

Assuming that the transmission power for each Tx antenna is 1, the MIMO channel capacity and the SNR at one of the subcarriers after whitening the noise are defined as follows:

$$C = \log_2 \det \left(\mathbf{I}_{N_r} + \tilde{\mathbf{H}} \tilde{\mathbf{H}}^H \right), \quad (6a)$$

$$\text{SNR} = \text{tr}(\tilde{\mathbf{H}} \tilde{\mathbf{H}}^H) / N_r. \quad (6b)$$

In addition to capacity and SNR, the bit error rate (BER) is also of interest. To evaluate this metric, we employ the expectation propagation-based (EP) MIMO detector [13] for both simulations and experiments.

For the simulations, we generate the elements of all the channel matrices, including \mathbf{H}_{los} , \mathbf{H}_{sm} , $\mathbf{H}_{\text{am}}^{\text{r}}$, and $\mathbf{H}_{\text{am}}^{\text{t}}$, based on the 3GPP spatial channel model (SCM) with antenna and polarization effects [8]. For the experiments, we have developed a prototype that is described in detail in the following subsection. This prototype allows us to validate the mentioned metrics through real-world scenarios.

C. Active RIS-Assisted MIMO System

In this subsection, we present the prototype of our active RIS-assisted 4T4R MIMO-OFDM system, as depicted in

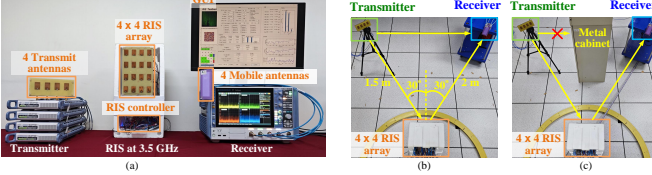


Fig. 2. (a) The prototype of the 4T4R MIMO-OFDM system assisted by the 4×4 active RIS array, and the experimental setup (b) with LoS and (c) without LoS.

Fig. 2(a), which can be categorized into three components: the transmitter (Tx), RIS, and receiver (Rx).

For the Tx, we transmit four-stream 5G OFDM signals in the 3.45-3.55 GHz band over the air. For our setup, we employ four one-port R&S vector signal generators, specifically the SGT100A model, which are connected to four transmit patch antennas. These antennas are positioned at intervals of half the wavelength corresponding to the 3.5 GHz frequency.

The RIS employs a 4×4 active RIS array, with an antenna structure similar to [8]. The detailed structure of each active RIS element is described in Section II-A. We use a DE10-Nano Kit, based on a Cyclone V SoC FPGA, as the RIS controller.

For the Rx, we receive the 5G signals using four mobile antennas, which are downconverted to the baseband using a four-port R&S digital oscilloscope, specifically the RTP164. The baseband signals are processed using a C program on a personal computer. Communication between the computer and the RIS controller takes place via a half-duplex Bluetooth connection, enabling the determination of the controlling strategy.

The framework of our MIMO-OFDM system in the baseband is as follows. The encoded data is converted to four-stream 5G signals using OFDM modulation. In our experiments, we utilize a bandwidth of 100 MHz with a subcarrier spacing of 60 kHz. The signals are subsequently upconverted to the 3.5 GHz band and transmitted. The receiver downconverts the received signals to the baseband, and synchronization is performed using 5G synchronization signal blocks. By performing channel estimation, we can calculate the capacity (6a) and SNR (6b) of the 4T4R MIMO-OFDM system. After performing the EP MIMO detector, we obtain the uncoded BER. It is important to note that our system adheres to the 5G NR standards, so the experimental performance and properties of the active RIS-assisted MIMO-OFDM system can be referenced in the context of 5G communications.

III. PROOF OF CONCEPT AND PERFORMANCE EVALUATION

A. Controlling Algorithms

To control the RIS, we employ the BG algorithm [8], which consists of two main steps: Random-Max Sampling (RMS) and Greedy Searching (GS). In RMS, a few codewords are drawn uniformly from an exhaustive codebook, and the best codeword is selected as the initial stage for the subsequent GS step. In GS, a progressive search is performed from the exhaustive states of each phase shifter, iterating through all the RIS elements. Instead of selecting the best received signal quality as in [8], we choose the RIS's state corresponding to the highest channel capacity in (6a) using the greedy method.

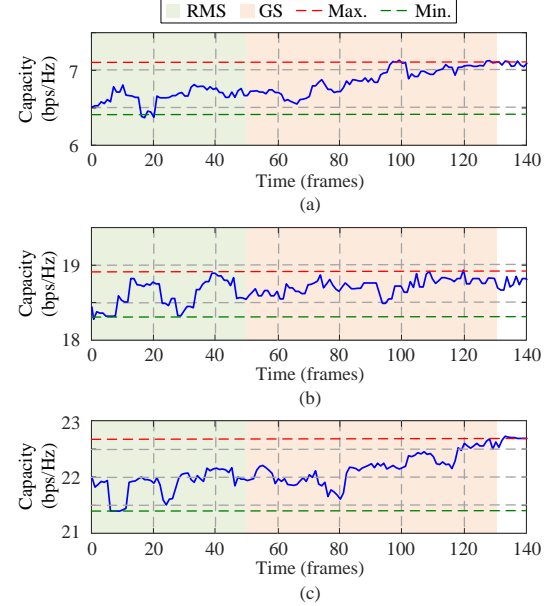


Fig. 3. Using BG, the state evolution of the controlling process for (a) passive RIS in the 1T4R OFDM system and the controlling process for (b) passive and (c) active RIS in the 4T4R MIMO-OFDM system.

In addition to the BG algorithm, we consider two other controlling algorithms for comparison. The first algorithm is CSM [7], which involves drawing uniformly from an exhaustive codebook and determining the RIS's state based on the phase expectation of each RIS element. We set the number of CSM's random samples to be 8 times the number of RIS elements.

The second algorithm is the conventional codebook-based algorithm, named the maximum-power codebook (MPC), which relies on the determined beam from the RIS. In MPC, we replace the Tx and Rx antennas in Fig. 2(b) with single horn antennas. With the RIS located at the center of the half circle with a radius of 2 m, we determine the RIS's codebooks by applying BG with the SNR in the SISO system to the Rx antenna locations along the half circle spaced by 5° . The determined codebooks, corresponding to different directions of RIS beams, are then utilized by MPC to select the best capacity among them in the MIMO system.

Note that the best RIS codeword in all the mentioned algorithms is determined by probing the capacity performance based on a set of codewords, and they do not require explicit channel matrix information. The performance of these algorithms depends on the number of probes, where a higher number of probes generally yields better performance. Therefore, their performances should be compared under the same number of probes.

B. Experiments

We conducted experimental measurements in an open area of the NSYSU Electrical and Computer (EC) Eng. Building to evaluate our active RIS-assisted MIMO-OFDM system. The setup, depicted in Fig. 2, involved placing the RIS at a distance of 1.5 m from the Rx and 2 m from the Tx. Two cases were considered: one where the LoS path was blocked by a metal

TABLE I
COMPARISON OF 4T4R MIMO SYSTEM IN THE DIFFERENT CASES.

Case	(64 QAM, w/o LoS)								(256 QAM, with LoS)				
	w/o RIS	(Passive, BG)			(Active, BG)			(Active, MPC)		w/o RIS	(Active, BG)		
	Initial	Best	Diff.	Initial	Best	Diff.	Best	Diff.	Initial	Best	Diff.		
SNR (dB)	18.23	18.55	18.88	0.45	21.40	22.93	1.61	22.01	1.29	24.40	25.10	25.26	0.21
Capacity (bps/Hz)	17.82	18.37	18.91	0.60	21.98	22.68	1.27	22.10	0.91	24.36	28.74	30.05	1.59
Uncoded BER	0.093	0.088	0.074	0.016	0.048	0.029	0.032	0.036	0.039	0.095	0.046	0.024	0.029
SE (bps/Hz)	- †	-	-	-	18.76	19.13	-	18.97	-	-	25.05	25.64	-

† If an uncoded BER is greater than 5e-2, SE will not be considered.

cabinet (Fig. 2(c)) and the other where it was not blocked (Fig. 2(b)).

To analyze the difference between passive RIS and active RIS in the BG controlling process, we present the state evolution of the controlling process in both the SIMO (1T4R) and MIMO (4T4R) systems in Fig. 3. Two levels of phase shift were chosen. The structure of the passive RIS was the same as described in [8]. In the SIMO system with the passive RIS, the capacity, as depicted in Fig. 3(a), undergoes significant changes during Random-Max Sampling (RMS) and shows a smooth increase during GS. However, in the MIMO system with the passive RIS, the capacity gain during GS, as shown in Fig. 3(b), is minimal. In contrast, when the passive RIS is replaced by the active RIS in the same scenario, the capacity gain during GS, as shown in Fig. 3(c), becomes more pronounced due to the use of amplifiers.

Furthermore, we compare the overall performance of the passive RIS and active RIS with and without the LoS path in Table I. The considered parameters include SNR, channel capacity, uncoded BER, and spectrum efficiency (SE). SE is defined as the throughput divided by the bandwidth. Our target is to achieve an uncoded BER of 5e-2, as a decoded BER using LDPC coding with a 1/2 code rate can approach 0 with this uncoded BER. To analyze the controlling process, we consider three types of RIS states, shown in Table I. The first type is the initial state before applying the BG algorithm. The second type is the final state after the BG algorithm, which corresponds to the best state of the RIS. The third type represents the difference between the best and worst states of the RIS encountered during the BG algorithm, which reflects the RIS's control ability. The performance of the initial RIS state falls between the performance of the best and worst RIS states.

In all cases without RIS, communication is not supported as the uncoded BER exceeds 5e-2. In the case without LoS, the passive RIS is not suitable for the MIMO-OFDM system as the performance gain is weak. However, even with the active RIS in the initial state, the performance gain is significant, and the BER can be reduced below 5e-2. Moreover, the improved controlling ability allows the MIMO-OFDM system to be more robust in different environmental conditions. To analyze the effect of multipath, we compare the BG algorithm with MPC, as MPC is similar to using RIS with beamforming techniques. The performance of MPC is worse than that of BG, and the final codebook of MPC corresponds to a different

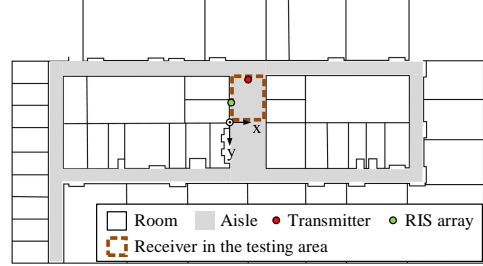


Fig. 4. Simulation environment.

beam expectation, specifically 45° instead of 30° in Fig. 2. This result indicates that considering the role of the RIS as a single-path assistance in MIMO scenario may not be appropriate. Finally, the controlling ability of SNR in the case with LoS (0.21 dB Diff.) is noticeably worse than that in the case without LoS (1.61 dB Diff.), as the SNR without RIS in the LoS case is much better than without RIS in the non-LoS case. However, the controlling ability of capacity remains significant, as the active RIS still has the ability to improve the multipath channel.

C. Simulations

To further analyze the properties of the RIS-assisted MIMO system, simulations are conducted using Wireless Insite® software, which incorporates the obtained channel impulse response into the channel model. The simulation environment, shown in Fig. 4, represents a scenario similar to the experiment described in Section III.B. The system corresponds to the 5G NR 4T8R MIMO-OFDM system, with Tx antennas oriented along the y-axis and RIS antennas facing along the x-axis. Four levels of phase shift without loss were considered, and the increased capacity was analyzed using the 68% inverse cumulative distribution function (ICDF) to reflect the receiver's improved performance in the testing area.

The performance of the RIS system is influenced by the size of the RIS array and the transmission gain Φ in (1). In Fig. 5, the capacity increase achieved by the BG algorithm is compared when using variable Φ^k or a fixed identical Φ for all RIS elements. Doubling the dimensions of the RIS array yields a performance similar to adding a total transmission gain of 6 dB due to the increased number of RIS elements. Additionally, the increased capacity of a 16 × 16 RIS array with 0 dB, representing a passive RIS, is comparable to that of a 2 × 2 active RIS array with an 18 dB power gain. These

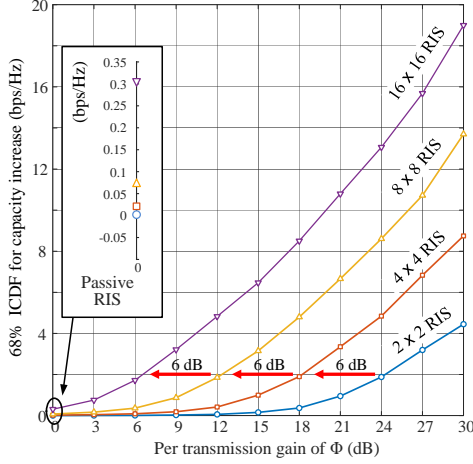


Fig. 5. Effects of the different RIS's total transmission gain for different sizes of square-arranged RIS arrays.

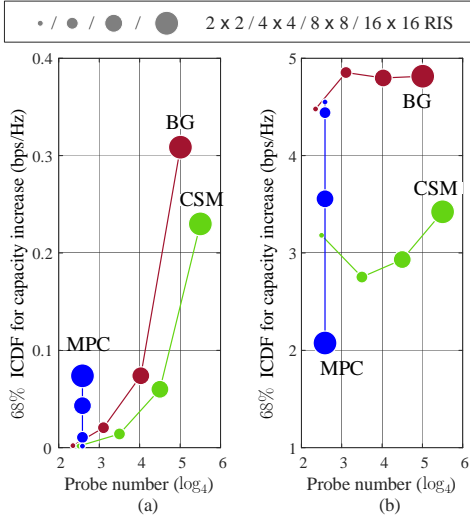


Fig. 6. Effects of different controlling algorithms for (a) passive RIS and (b) active RIS.

findings highlight the potential benefits of reducing the size of the RIS while considering the associated energy costs.

To analyze the effects of different controlling algorithms, we consider their probe numbers and capacity increase. The results for passive and active RIS arrays of different sizes are shown in Figs. 6(a) and 6(b) respectively. The probe number is presented using a base-4 logarithm, and the maximum number of probes depend on the number of RIS elements. In the figure, a larger value on the x-axis indicates a longer searching time, while a larger value on the y-axis represents higher algorithm performance. Therefore, the most efficient algorithm should ideally appear in the top-left corner, where it achieves high performance with a short search time.

For the passive RIS, the capacity growth with increasing RIS array size is significantly smaller for MPC compared to the other algorithms, even with a fixed number of probes. Additionally, CSM requires a larger number of random probes to achieve good performance, resulting in higher complexity compared to the other algorithms. In fact, none of the algo-

rithms belong to the top-left corner, implying their inefficiency in the context of the passive RIS.

Regarding the active RIS, we impose a restriction on the sum of the total transmission gains, limiting it to 36 dB. For instance, the total transmission gains for a 2×2 and a 16×16 RIS array are 30 dB and 12 dB, respectively. As the number of RIS elements increases, the capacity increase achieved by MPC diminishes. This outcome suggests that the conventional beamforming-based codebook, which focuses solely on optimizing a single path, is insufficient for the MIMO system. These findings align with the experimental results presented in Table I. Moreover, small active RISs, which belong to the top-left corner of the performance plot, prove to be an efficient choice in the context of the MIMO system.

IV. CONCLUSION

This study presented the first experimental development of active RIS-assisted MIMO-OFDM in the 5G NR context, featuring practical base station and smartphone form factors. The results demonstrated the crucial role of active RIS in improving MIMO systems. We showed that the conventional beamforming-based codebook is insufficient for the MIMO system, emphasizing the need for a smarter controlling algorithm. From a practical perspective, a smaller active RIS demonstrated greater potential compared to a larger passive RIS.

REFERENCES

- [1] L. Dai *et al.*, “Reconfigurable intelligent surface-based wireless communications: Antenna design, prototyping, and experimental results,” *IEEE Access*, vol. 8, pp. 45 913–45 923, 2020.
- [2] X. Pei *et al.*, “RIS-aided wireless communications: Prototyping, adaptive beamforming, and indoor/outdoor field trials,” *IEEE Trans. Commun.*, vol. 69, no. 12, pp. 8627–8640, 2021.
- [3] R. Fara *et al.*, “A prototype of reconfigurable intelligent surface with continuous control of the reflection phase,” *IEEE Wirel. Commun.*, vol. 29, no. 1, pp. 70–77, 2022.
- [4] M. Dunna *et al.*, “ScatterMIMO: Enabling virtual MIMO with smart surfaces,” in *in Proc. 26th Ann. Int. Conf. Mobile Computing and Networking (MobiCom’20)*, New York, NY, USA, 2020, pp. 1–14.
- [5] A. Araghi *et al.*, “Reconfigurable intelligent surface (RIS) in the sub-6 GHz band: Design, implementation, and real-world demonstration,” *IEEE Access*, vol. 10, pp. 2646–2655, 2022.
- [6] J. Sang *et al.*, “Coverage enhancement by deploying RIS in 5G commercial mobile networks: Field trials,” *IEEE Wirel. Commun.*, pp. 1–21, 2022.
- [7] S. Ren *et al.*, “Configuring intelligent reflecting surface with performance guarantees: Blind beamforming,” *IEEE Trans. Wireless Commun. (Early Access)*, Nov. 2022.
- [8] D.-M. Chian *et al.*, “A novel channel model for reconfigurable intelligent surfaces with consideration of polarization and switch impairments,” 2023. [Online]. Available: <https://arxiv.org/abs/2304.03713>
- [9] Z. Kang, C. You, and R. Zhang, “Active-RIS-aided wireless communication: Fundamentals, designs and open issues,” 2023. [Online]. Available: <http://arxiv.org/abs/2301.04311>
- [10] R. Long *et al.*, “Active reconfigurable intelligent surface-aided wireless communications,” *IEEE Trans. Wireless Commun.*, vol. 20, no. 8, pp. 4962–4975, 2021.
- [11] Z. Zhang *et al.*, “Active RIS vs. passive RIS: Which will prevail in 6G?” *IEEE Trans. Commun.*, vol. 71, no. 3, pp. 1707–1725, 2023.
- [12] ———, “Active RISs: Signal modeling, asymptotic analysis, and beamforming design,” in *2022 IEEE Global Communications Conf.*, Rio de Janeiro, Brazil, Dec. 2022, pp. 1618–1624.
- [13] J. Zhang, C.-K. Wen, and S. Jin, “Adaptive MIMO detector based on hypernetwork: Design, simulation, and experimental test,” *IEEE J. Sel. Areas Commun.*, vol. 40, no. 1, pp. 65–81, 2022.